Front. Energy 2025, 19(6): 949–968
https://doi.org/10.1007/s11708-025-1028-y

RESEARCH ARTICLE

Numerical study of a parabolic-trough CPV-T collector with spectral-splitting liquid filters

Chandan Pandey[1], Mingyang Wu[1], Adelani Oyeniran[1], Sandesh S. Chougule[1,2], Ivan Acosta Pazmiño[3], Carlos I. Rivera-Solorio[3], Miguel Gijón-Rivera[4], Christos N. Markides (✉)[1]

1 Clean Energy Processes (CEP) Laboratory, Department of Chemical Engineering, Imperial College London, London SW7 2AZ, UK
2 Solar Flow Ltd., London SW11 3BQ, UK
3 Tecnologico de Monterrey, Institute of Advanced Materials for Sustainable Manufacturing, Av. Eugenio Garza Sada 2501, Monterrey, N.L, 64849, Mexico
4 Tecnologico de Monterrey, Escuela de Ingeniería y Ciencias, Vía Atlixcáyotl 5718, Reserva Territorial, Atlixcáyotl, Puebla 72453, PUE, México

© The Author(s) 2025. This article is published with open access at link.springer.com and journal.hep.com.cn

Abstract Conventional flat-plate photovoltaic-thermal (PV-T) collectors generate electricity and heat simultaneously; however, the outlet temperature of the latter is typically below 60 °C, limiting their widespread application. The use of optical concentration can enable higher-temperature heat to be generated, but this can also lead to a rise in the operating temperature of the PV cells in the collector and, in turn, to a deterioration in their electrical performance. To overcome this challenge, an optical spectral-splitting filter that absorbs the infrared and transmits the visible portion of the solar spectrum can be used, such that wavelengths below the bandgap are sent to the cells for electricity generation, while those above it are sent to a thermally decoupled absorber for the generation of heat at a temperature that is considerably higher than that of the cells. In this study, a triangular primary PV-T channel, wherein the primary heat transfer fluid (water) flows, is integrated into a parabolic trough concentrator of geometrical concentration ratio ~10, while a secondary liquid filter (water, $AgSiO_2$-eg or Therminol-66) is introduced for spectral splitting. Optical, electrical and thermal-fluid (sub-)models are developed and coupled to study the performance of this collector. Each sub-model is individually checked against results taken from the literature with maximum deviations under 10%. Subsequently, the optical and electrical models are coupled with a 3-D thermal-fluid CFD model (using COMSOL Multiphysics 6.1) to predict the electrical and thermal performance of the collector. Results show that when water is used as the optical filter, the maximum overall thermal (filter channel plus primary channel) and electrical efficiencies of the collector reach ~45% and 15%, respectively. A comparison between water, $AgSiO_2$-eg and Therminol-66 reveals that $AgSiO_2$-eg improves the thermal efficiency of the filter channel by ~25% (absolute) compared to Therminol-66 and water, however, this improvement – which arises from the thermal performance of the filter – comes at an expense of a ~5% electrical efficiency loss.

Keywords concentrator, filter, photovoltaic-thermal, solar energy, spectral splitting

1 Introduction

Solar energy utilisation is a key element of all energy transition and net zero pathways [1], with sustained progress being made globally via the deployment of both solar photovoltaic (PV) and solar thermal technologies. PV modules convert solar radiation into electricity directly [2], whereas solar thermal collectors use sunlight to heat up a heat transfer fluid (HTF), thereby providing a useful thermal energy output [3,4]. Most installed solar thermal collectors are based on flat-plate or evacuated-tube [5,6] designs aimed at providing low-temperature hot water for domestic consumption, however, other (e.g., concentrating [7,8]) collector designs are also available, for this and also other applications. The potential for cost reduction and performance improvement offers new opportunities in combining solar PV and solar thermal components in hybrid photovoltaic-thermal (PV-T) technologies [9–12], which have overall (electrical plus thermal) efficiencies that can be 2–3 times those of standalone solar PV panels [13].

Received Oct. 28, 2024; accepted Apr. 9, 2025; online Jul. 25, 2025
Correspondence: Christos N. Markides, c.markides@imperial.ac.uk

Despite their simple structure and low maintenance, the outlet temperature of the HTF in conventional, flat-plate PV-T collector design is relatively low [14], making this technology better suited to low-temperature domestic hot-water provision rather than higher-grade process heat applications. This limitation of a low-grade thermal output from non-concentrating PV-T collectors is overcome by concentrating PV-T (CPV-T) collectors [15–20]. Recently, CPV-T collectors have found various applications in the heating industry. For example, integrating phase change materials (PCM) in CPV-T collectors for heat storage has been shown to promote the supply of heat to residential buildings for different scenarios [21]. Furthermore, Leonforte et al. [22] integrated a heat pump with a CPV-T collector and demonstrated that this combination could boost the heat pump's seasonal performance as well as decrease the reliance on electricity from the grid. CPV-T collectors can also be applied in the industrial sector associated with industrial heating [23], waste heat recovery [24], and desalination [25].

Although CPV-T co-generation designs have numerous benefits, they are not without some drawbacks. As electricity and heat are generated simultaneously, a coupling between these two outputs is unavoidable which tends to limit the electrical efficiency. To address the limitation in conventional CPV-T collectors, advanced thermal management techniques, such as spectral splitting (SS) [26], have been explored. In SS collector designs, the incident solar radiation is separated such that the visible part of the spectrum reaches the solar PV cells [26], while the ultraviolet (UV) and infrared (IR) parts are reflected or absorbed by a filter. SS technology partially decouples the electrical and heat generation, which subsequently improves the thermal performance of the collector without affecting its electrical performance [27].

To-date, numerous studies have assessed the efficiency of various spectral splitting CPV-T (SSCPV-T) collectors using liquid absorptive filters. Huang et al. [28] numerically examined the spectral distribution and energy allocation between spectral bands by changing the spectral window size of the liquid absorptive filter, with the upper boundary held constant at 1100 nm (band gap of c-Si), and the lower boundary varied from 400 to 800 nm. One finding from this work concerned the rapid increase of the absorbed energy by the liquid filter as the lower boundary increased, with the fraction increasing from 25% to 70% of the total solar energy, while the electrical output decreased from 19% to 7%. The results indicated that finding a proper wavelength range of the filter can enhance the overall energy output depending on the application.

In another study, Han et al. [29] proposed a combined liquid absorptive filter, leveraging the optical characteristics of propylene glycol (PG) and HB650 glass. PG was employed in the filter channel to absorb the wavelengths above 1300 nm, while HB650 was used as the inner tube material to absorb wavelengths below 650 nm. The authors then investigated the electrical and thermal efficiencies as well as the potential economics of this CPV-T collector. It was reported that 72% of the solar energy (from 650 to 1075 nm) could be utilised upon adopting the proposed combined liquid filter. This new design enabled the collector to reach a maximum thermal efficiency of 41%, however, the electrical efficiency consequently dropped to half of the original value. Additionally, the new design was anticipated to yield 54% more economic value compared with a conventional benchmark PV system.

Han et al. [30] measured the optical transmittance of $Ag/CoSO_4$ nanofluids, with $CoSO_4$ used as the base fluid (40 g/L). Thermodynamic and optical analyses were performed for a CPV-T hybrid system with an optical splitter and fully tracked linear Fresnel reflector concentrator utilising sloped panels and three mass fractions of Ag nanoparticles (84.7, 31.8, and 5.3 ppm). It was demonstrated that the use of $Ag/CoSO_4$ nanofluids had strong absorption over a broad spectrum (340–595 nm), indicating a suitability for use with c-Si solar cells.

Barthwal and Rakshit [31] performed simulations to evaluate the use of ZnO nanofluids as liquid absorptive filters. It was found that the use of ZnO nanofluids can enable a substantial reduction in the PV cell operating temperature, with an average temperature decrease of close to 50 K, which is beneficial for the performance and lifetime of the cells. It was also demonstrated that the electrical efficiency of the SSCPV-T collector was maintained at 18% at solar noon in June, while the conventional design suffered from a significant loss in electrical efficiency due to the drastic temperature increase. Table 1 shows a selection of state-of-the-art studies in the field.

Although previous studies have made significant contributions toward the advancement of SSCPV-T technology, little attention has been paid to establishing fully coupled numerical models of such collectors. The aim of the present study was to develop a full 3-D model of a proposed SSCPV-T collector design that integrates optics, heat transfer and fluid dynamics using COMSOL Multiphysics 6.1 [50]. The optical sub-model, which was developed using ray tracing, accounts for the spectral distribution of the incident solar radiation (i.e., as a function of wavelength), while considering a liquid filter as a spectral splitting material. An in-house MATLAB (version R2022a) [51] code was also developed to predict the electrical performance of the collector. The net flux obtained from the optical sub-model minus the electrical power output obtained from the MATLAB code is used as a uniform (local flux distribution averaged over the circumferential length) heat source. Coupled with a computational fluid dynamics (CFD) sub-model of the fluid channels, these outputs are used to estimate the

Table 1 State-of-the-art SS-based CPV-T collectors

Year	Author	Filter type	Filter material	Concentrator	PV type
2014	Liu et al. [32]	Interference	TiO_2 layers	Linear Fresnel reflector	c-Si
2014	Looser et al. [33]	Absorptive	Propylene glycol with red dye	Micro concentrator	c-Si
2015	Mojiri et al. [34]	Absorptive	Propylene glycol	Parabolic trough	c-Si
2015	Mojiri et al. [35]	Hybrid	Dichroic mirror, water Propylene glycol Ethylene glycol	Linear micro concentrator	c-Si
2016	Stanley et al. [36]	Hybrid	Propylene glycol Bandpass optical filter	Parabolic trough	c-Si
2018	Widyolar et al. [37]	Interference	Dichroic mirror	Parabolic trough	c-Si
2018	Joshi and Dhoble [38]	Absorptive	Water Silicone oil	Parabolic dish	c-Si
2019	Han et al. [39]	Absorptive	Coconut oil Inorganic aqueous salt Glycol Silicone oil Synthetic oil Mineral oil	Non-concentrating	c-Si/ GaAs
2019	Li et al. [40]	Absorptive	Ag/TiO_2 nanoparticles	Non-concentrating	c-Si
2020	Wingert et al. [41]	Interference	Dichroic mirror	Parabolic trough	c-Si
2020	Yazdanifard et al. [42]	Absorptive	PCM nanofluid	Not mentioned	c-Si
2020	Ling et al. [43]	Interference	Multiple layers of Ta_2O_5/SiO_2	Linear Fresnel reflector	CdTe
2022	Barthwal and Rakshit [31]	Absorptive	ZnO nanofluid	Compound parabolic collector	c-Si
2022	Alnajideen and Min [44]	Interference	Dichroic mirror	V-trough	GaInP
2022	Wang et al. [45]	Absorptive	Indium tin oxide-ethylene glycol nanofluid	Parabolic trough	c-Si
2022	Meraje et al. [46]	Absorptive	ZnO nanofluid	Fresnel lens	c-Si
2023	Li et al. [47]	Interference	TiO_2–Na_3AlF_6	Parabolic dish	GaAs
2023	Zhang et al. [48]	Interference	Multilayer polymer film	Parabolic trough	c-Si
2024	Chougule et al.[49]	Absorptive	Ag-ZnO	Non-concentrating	c-Si

electrical and thermal performance of the SSCPV-T collector. Finally, the coupled optical, electrical, and thermal sub-models are used to generate a performance map of the proposed SSCPV-T collector. A comparative study of different liquid filters was also performed.

2 Collector design

Detailed dimensions and a description of key components of the SSCPV-T collector are provided in Fig. 1. The collector is based on an existing commercial parabolic trough concentrator used in solar thermal applications, manufactured by a Mexican company Inventive Power [52]. The concentrator was installed, and it is still in operation, in Tec de Monterrey (Mexico), and all the dimensions of the concentrator were measured directly for accuracy. The objectives in this study were to hybridise a commercial parabolic-trough solar thermal collector and to convert this to a CPV-T collector by modifying the receiver and installing PV cells, and to explore the technical (i.e., electrical and thermal) performance of the hybrid collector after implementing a spectral-splitting design, specifically introducing a selective-absorptive-based optical SS filter between the reflector and the solar cells on the receiver, which takes the form of a triangular channel through which the primary HTF flows.

In Fig. 1, the origin of the x–y plane coincides with the vertex of the parabolic reflector. The x-axis is tangential to the illuminated surface of the parabola at the vertex (O), while the y-axis is perpendicular to the x-axis, which is also the axis of symmetry for the parabola. The z direction is defined as being along the length of the collector, which is also the direction of flow. The equation of the linear parabolic concentrator is given below in parametric form:

$$x^2 = 4fy,$$

$$\begin{cases} x = 2ft, \\ y = ft^2, \end{cases} \quad (1)$$

where f is the focal length, and t ($\in$ [–0.8, 0.8]) is a parameter that defines the reflector's shape.

Furthermore, the outer diameter of the glass envelope in the collector is 100 mm, with a thickness of 2.2 mm. The glass envelope is made of low-iron glass whose optical parameters are discussed in Section 3.1. An equilateral triangular receiver also referred to as the primary PV-T channel, whose center is aligned with the center of the glass envelope, is placed inside it. The solar

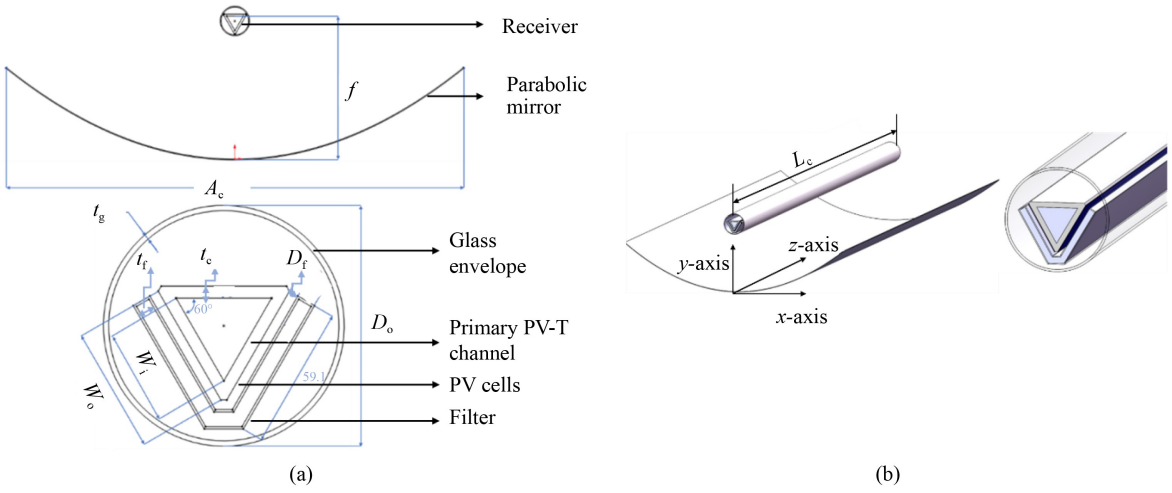

Fig. 1 SSCPV-T collector.
(a) Cross-sectional view; (b) 3-D model. (The PV cells are on the two sloped, flat sides of the central primary PV-T channel.)

PV cells are attached to the primary PV-T channel (as shown in Fig. 2). The width of the outer surface is 52 mm, and the width of the inner surface is 40 mm, with a thickness of 5 mm. The length of the collector is 3000 mm. Key dimensions are summarised in Table 2.

In this SSCPV-T collector, a parabolic mirror is positioned to focus the incident solar radiation onto the receiver located at its focal point. When the incident rays meet the mirror, they are reflected and directed toward the receiver where ~90% of this radiation is transmitted through the glass envelope of the receiver, while the rest is either reflected or absorbed. Thereafter, the transmitted rays first reach the liquid absorptive filter where the UV and IR parts of the spectrum are absorbed; the remaining wavelengths penetrate the filter and reach the PV cells, which convert this (part of the) sunlight to both electricity and heat. The electricity is delivered by connecting wires, while the heat is extracted from the back of the PV cells with the primary PV-T fluid channel. In summary, this SSCPV-T collector generates electricity, high-temperature heat in the filter channel, and low-temperature heat in the primary PV-T channel. A schematic of the energy flows at the receiver is shown in Fig. 3.

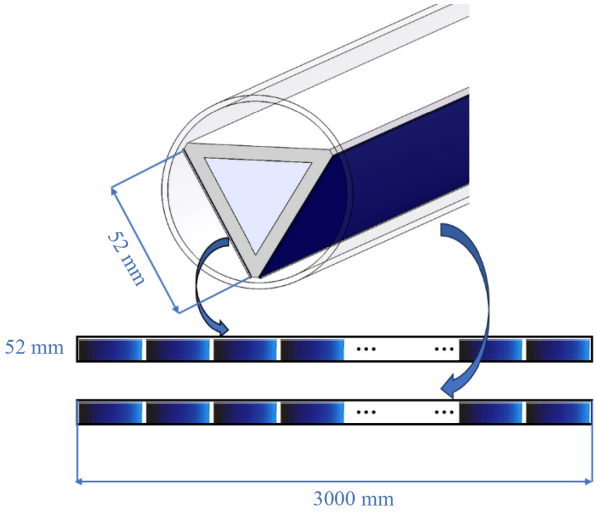

Fig. 2 Dimensions and arrangement of the customised solar cells used in this work.

Table 2 Dimensions of the SSCPV-T collector as presented in Fig. 1

Parameter	Value/mm
Aperture width (A_c)	1088
Focal length (f)	340
Glass envelope outer diameter (D_o)	100
Glass envelope thickness (t_g)	2.2
Primary PV-T channel width (outer) (w_o)	52
Primary PV-T channel width (inner) (w_i)	40
Primary PV-T channel wall thickness (t_c)	5
Gap between filter and channel (D_f)	4
Liquid filter thickness (t_f)	6
Collector length (L_c)	3000

3 Methods

In this section, details on the optical, electrical and thermal-fluid models are provided. For the optical model, laws of reflection and refraction are applied for ray tracing and estimating the flux received by the filter and solar cells. For the electrical model, a MATLAB code has been developed that assumes an AM1.5G solar spectrum and uses the spectral response of a commercial c-Si PV cell, and the transmittance of the filter material to estimate electrical performance at the appropriate

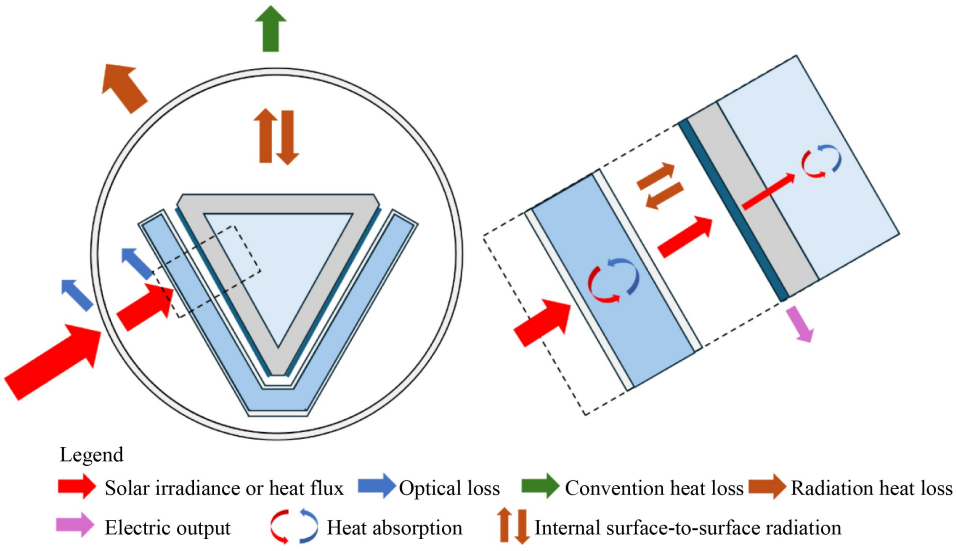

Fig. 3 Energy flow diagram in the SSCPV-T receiver.

operating temperature. The optical and electrical models are coupled to a computational fluid dynamics (CFD) model where mass, momentum and energy conservation equations are solved to estimate the thermal performance of the collector.

3.1 Optical model

The following assumptions are made in the optical model:

- Solar rays are parallel, and the solar disk radial angle is ignored in the simulation.
- All surfaces are smooth; hence, the scattering effect are neglected.
- Optical materials are homogeneous.

The solar irradiance is reflected by the parabolic concentrator toward the surface of the solar cells, increasing the solar flux intensity on the cells. The reflectance of the parabolic trough collector considered in this study is 93% [53]. Subsequently, the reflected light passes through the cover glass and optical filter before reaching the solar cells. The transmittance of the cover glass and filter glass (clean state) are assumed to be 91% [54] in the simulations. After this, only a fraction of solar irradiance is converted to electrical energy, while the rest is converted to thermal energy in the cells. In this simulation, the optical simulation was used to estimate the local flux received at the filter and the primary PV-T channel. Subsequently, the local fluxes obtained at the filter and the primary PV-T channel were averaged along the corresponding circumferential lengths and used as uniform heat flux inputs to the CFD model. The optical properties of the collector are given in Table 3, with the overall solar spectrum that is received by the cells described by:

Table 3 Optical properties of collector components

Optical properties	Value
Collector reflectance (ρ_c)	0.93
Low-iron glass transmittance (τ_g)	0.91
Solar cells cover glass transmittance (τ_{cg})	0.91
Solar cell absorptivity (α_{pv})	0.92

$$G_{pv}(\lambda) = G_{AM1.5}(\lambda)\rho_c\tau_g\tau_{fl}(\lambda), \quad (2)$$

where $G_{AM1.5}(\lambda)$ and $G_{pv}(\lambda)$ are the incident solar radiation spectrum (in W/(m^2·nm)) and the solar spectrum received by the cells (in W/(m^2·nm)), ρ_c the reflectivity of the mirror, τ_g the transmittivity of the glass, and $\tau_{fl}(\lambda)$ the transmittivity of the filter as a function of wavelength. The AM1.5G spectrum is shown in Fig. 4(a), and the transmittance profiles of water [55] $AgSiO_2$-eg nanofluid [56] and Therminol-66 [57], which are the three liquids considered for the SS filter, are shown in Fig. 4(b).

3.2 Electrical model

The following assumptions are made for the electrical model:

- The C60 mono-crystalline solar cell is considered to behave as an ideal diode.
- The shunt resistance and series resistance are negligible.
- The concentrated solar flux is uniformly distributed over the PV surface.

The dark saturation current density generated by the solar PV cells is given by [13]:

$$J_{ds} = k_1 T_{std}^{\frac{3}{\tau}} \exp\left(\frac{-E_{bg}}{bk_B T_{std}}\right), \quad (3)$$

where J_{ds} is the dark saturation current density, E_{bg} the

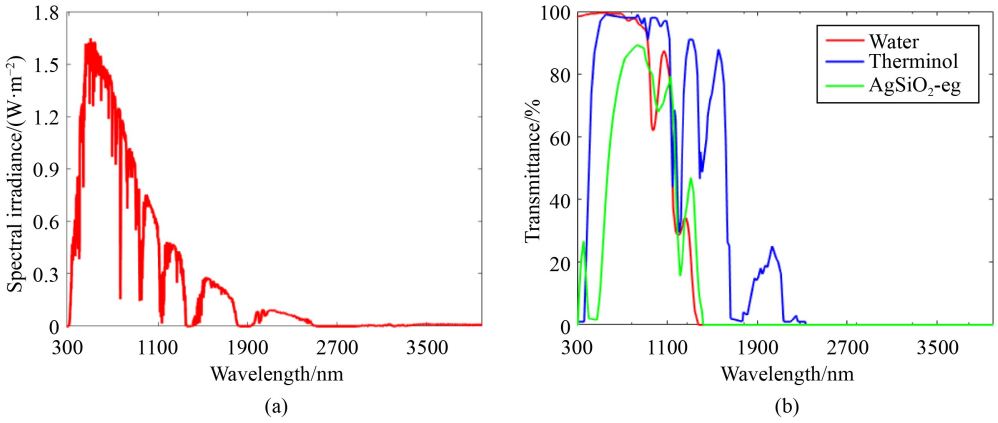

Fig. 4 (a) AM 1.5G spectrum; (b) transmittance profile of the three investigated optical filter fluids: water, $AgSiO_2$-eg and Therminol-66.

solar cell band gap energy, T_{std} the standard temperature, and k_B the Boltzmann constant, the value of which can be found in Table 4. In addition, k_1, b, and z are empirical parameters, and their values are 0.03, 1.25, and 0.98, respectively [13]. The short circuit current density, which represents the maximum current that a solar PV cell can draw in the no-load condition, is given by [13,28]:

$$J_{sc} = C_{geo}\int_{280}^{4000} G_{pv}(\lambda)SR(\lambda)\mathrm{d}\lambda, \tag{4}$$

where J_{sc} is the short circuit current density, and $SR(\lambda)$ the cell spectral response, which is defined as the ratio of the current generated at a specific wavelength to the incident power on the cell. For this study, we use the spectral response of the SunPower C60 solar cell [58] available in the datasheet provided by manufacturer; the response is shown in Fig. 5.

The short circuit current, which is the maximum current that can flow through the cell with its terminals shorted, can be obtained by multiplying J_{sc} with the solar cell area (A_{cell}):

$$I_{sc} = J_{sc}A_{cell}. \tag{5}$$

The open circuit voltage, which is the maximum voltage across a single solar cell under no load conditions, is given by:

$$V_{OC} = \frac{A_i k_B T_{std}}{e}\ln\left(\frac{J_{sc}}{J_{ds}}+1\right), \tag{6}$$

where V_{oc} is the open circuit voltage, e the unit charge and A_i the ideality factor of the solar PV cell. The ideality factor accounts for the recombination losses caused due to the recombination of the electron-hole pair in the solar PV cell and is assumed to be 1.18 in this work.

The maximum power point (MPP) describes the point where a PV module delivers maximum power and can be described as the product of I_{sc}, V_{oc} and fill factor (FF):

$$FF = \frac{v_{oc} - \ln(v_{oc}+0.72)}{v_{oc}+1}, \tag{7}$$

$$v_{oc} = \frac{e}{A_i k_B T_{std}}V_{oc}, \tag{8}$$

where v_{oc} is the normalised open-circuit voltage. A summary of parameters and other constants used in the electrical model is provided in Table 4.

The use of the liquid filter can alter the spectral irradiance that falls on the PV surface, hence the system-level electrical efficiency. The electrical efficiency in this study is defined as [13]:

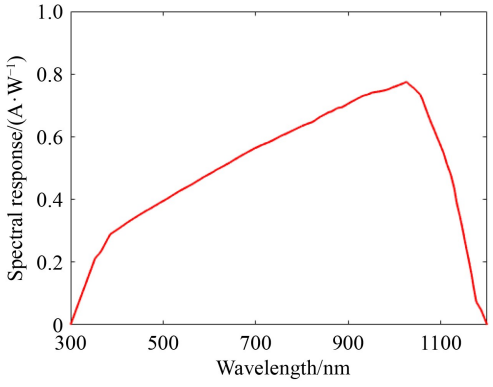

Fig. 5 SunPower C60 mono-crystalline solar cell spectral response [58].

Table 4 Electrical model constants

Symbol	Constants	Value	Unit
k_B	Boltzmann constant	1.38×10^{-23}	J/K
T_{std}	Standard temperature	298.15	K
E_{bg}	Band gap energy	1.1	eV
k_1	Empirical parameter	0.03	–
b	Empirical parameter	1.25	–
z	Empirical parameter	0.98	–
e	Electron charge	1.6×10^{-19}	C
h	Planck's constant	6.6×10^{-34}	J·s
c	Light speed	3×10^{8}	m/s
A_i	Ideality factor	1.18	–

$$\eta_{el} = \frac{V_{oc} I_{sc} FF}{G_{AM1.5} A_c} [1 - \beta(T_{pv} - T_{std})], \quad (9)$$

which accounts for temperature variations for operation away from standard conditions (25 °C).

Data provided by the manufacturer and generated from the MATLAB code is presented in Table 5. Simulation results align with the manufacturer's data with a maximum error of < 4%.

Table 5 Physical and electrical characteristics of C60 mono-crystalline solar cell from the manufacturer (SunPower) and MATLAB code simulation

Parameter	Manufacturer	MATLAB code	Error
Dimensions	125 mm × 125 mm		–
Thickness	165 ± 40 μm		–
β	–0.32%/ °C		–
V_{oc}	0.687 V	0.673 V	2%
I_{sc}	6.28 A	6.51 A	4%
η_{el}	22.5%	23.1%	2%

The standard dimensions of the SunPower C60 mono-crystalline solar cell are not suitable for installation on the receiver, thus in this study, the cell dimensions were customised (52 mm × 125 mm). A schematic of the solar cell arrangement is shown in Fig. 2, which shows 2 strings of solar cells attached onto the surface of the primary PV-T channel with 48 cells in total.

3.3 Flow and heat transfer model

The following assumptions are made in the collector's solid and fluid components/domains:

- The system is considered to have reached steady-state conditions ($\partial T/\partial t = 0$).
- The impact of thermal expansion is neglected, and the thermoelastic effect in the solid material (thermoelastic damping) is ignored.
- The thermal contact resistance between the PV cells and the thermal absorber (primary PV-T channel) is ignored.
- The flow is incompressible, and the density remains constant throughout the flow ($\partial\rho/\partial x = \partial\rho/\partial y = \partial\rho/\partial z = 0$).
- A single-phase model approach is considered for the nanofluid used in the filter.
- The effect of gravity is neglected.

In COMSOL, the steady-state differential form of the heat conduction equation is implemented in all solid domains (glass layers and the aluminum channel), which is given by:

$$\nabla \cdot (\vec{q} + \vec{q}_r) = k_s \left(\frac{\partial^2 T}{\partial x^2} + \frac{\partial^2 T}{\partial y^2} + \frac{\partial^2 T}{\partial z^2} \right) + \nabla \cdot \vec{q}_r = 0, \quad (10)$$

where $\vec{q}$ and $\vec{q}_r$ are conduction and radiation heat flux vectors, the latter only for transmission of radiation through the solid, and k_s is the thermal conductivity for the given solid material.

Likewise, a steady-flow energy equation is solved in the fluid domains:

$$\rho c_p \vec{u} \cdot \nabla T + \nabla \cdot \vec{q} = q_{fl} + q_{vd}, \quad (11)$$

where the term q_{vd} is a viscous dissipation (heating) term, which is enabled in the COMSOL Multiphysics field interface. In addition, q_{fl} denotes the heat flux absorbed by the filter, which is modeled by the boundary heat source interface in COMSOL.

The Reynolds number is crucial for determining the state of the flow in the collector [59]:

$$Re = \frac{\rho U D_H}{\mu}, \quad (12)$$

where U is the mean (bulk) velocity of the fluid, ρ and μ are the density and dynamic viscosity of the fluid, and D_H the hydraulic diameter:

$$D_H = \frac{4A_{cs}}{P_w}, \quad (13)$$

where A_{cs} denotes the cross-section area, and P_w the wetted perimeter of the channel.

In the present work, *Re* of the flow was varied from 60 (laminar) to 3900 (turbulent).

Finally, the continuity equation is an expression of mass conservation. For single-phase incompressible flow, conservation of mass is given by [59]:

$$\nabla \cdot (\rho \vec{u}) = \frac{\partial u}{\partial x} + \frac{\partial u}{\partial y} + \frac{\partial u}{\partial z} = 0, \quad (14)$$

and momentum conservation can be written as:

$$\rho (\vec{u} \cdot \nabla) \vec{u} = \nabla \cdot \left[-p \vec{I} + \vec{\tau} \right] + \vec{F}, \quad (15)$$

where $\rho(\vec{u} \cdot \nabla)\vec{u}$ is the convective term, $-\nabla p$ the pressure term, $\nabla \cdot \vec{\tau}$ the viscous term, and $\vec{F}$ denotes any external forces; here, gravity is neglected such that $\vec{F} = 0$.

The model accounts for radiation heat loss: (a) radiation exchange between internal surfaces, such as the outer surfaces of the filter glass, PV cells, and the inner layer of the glass envelope of the receiver, and (b) radiation heat loss to the sky from the outer layer of the glass envelope. The radiation exchange inside the receiver is given by [59]:

$$q_{1\to 2} = J_1 \iint \frac{\cos\theta_1 \cos\theta_2 \, dA_1 \, dA_2}{\pi R^2}, \quad (16)$$

where $q_{1\to 2}$ represents the radiation heat transfer from Surface 1 to Surface 2, with the surfaces having differential areas dA_1 and dA_2, J_1 is the radiosity assumed to be uniform over the differential area dA_1, and θ describes the angle between the surface normal and the line of length R that connects two differential areas dA_1 and dA_2.

The fraction of radiation that leaves surface A_1 and intercepted by surface A_2 is given by:

$$F_{12} = \frac{q_{1\to 2}}{A_1 J_1} \text{ and } A_1 F_{12} = A_2 F_{21}, \tag{17}$$

where F_{12} is the view factor between two surfaces that are diffuse emitters.

In this study, two non-isothermal flow interfaces in the channel and the filter are employed. The fluid flow is coupled with the heat transfer using non-isothermal flow. Also, the surface-to-surface radiation interface is enabled to couple the radiation with heat transfer in the vacuum tube. Note that the convection and radiation losses at the outer surface of the glass envelope are implemented by the boundary conditions that will be discussed in this section below. Parameters utilised in the thermal-fluid model are summarised in Table 6.

The thermophysical properties of water, $AgSiO_2$-eg and Therminol-66 are considered as being temperature dependent, and were estimated using the expressions given in Table 7.

The initial temperature of the collector is set to 25 °C. The inlet flow velocities are governed by the Dirichlet (first type) boundary condition, where the mass flow rates are specified in this study. The pressure is set to zero for the outlet boundaries of both the channel and the filter to measure the pressure drop. In addition, backflow suppression is also activated.

Table 6 Thermophysical properties used in the thermal-fluid model

Materials	Density/ ($kg·m^{-3}$)	Thermal conductivity/ ($W·(m·K)^{-1}$)	Specific heat capacity/ ($J·(kg·K)^{-1}$)
Low-iron glass	2530	0.937	730
Aluminium	2700	238	900

As previously stated in the heat transfer governing equations, the solar irradiance absorbed by the filter and PV cells is employed using boundary heat source terms:

$$q_{pv} = \int_{280}^{4000} G_{pv}(\lambda)\,d\lambda, \tag{18}$$

$$q_{fl} = \int_{280}^{4000} G_{fl}(\lambda)\,d\lambda, \tag{19}$$

where $G_{pv}(\lambda)$ and $G_{fl}(\lambda)$ are the spectral irradiance received by the solar cell and by the filter whereas q_{pv} and q_{fl} are the irradiance absorbed by the PV cells and by the filter, respectively.

The heat generated in the solar cells is:

$$q_g = \alpha_{pv} q_{pv} - \eta_{el} C_{geo} G_{AM1.5}, \tag{20}$$

where α_{pv} is the absorptivity of the solar cells, C_{geo} the geometrical concentration ratio, and $G_{AM1.5}$ the incident solar irradiance on the aperture of the collector.

A convective heat loss is included in the model using the convective heat flux at the outer surface of the glass envelope and specifying an ambient temperature, assumed to be 25 °C:

$$q_{conv} = h_{wind}(T - T_{amb}), \tag{21}$$

where q_{conv} is the heat flux lost to the ambient by convective heat transfer, and h_{wind} the convective heat transfer coefficient that can be determined from [61]:

$$h_{wind} = 5.7 + 3.8 V_{wind}, \tag{22}$$

with V_{wind} the wind speed, which in this study is assumed to be 1 m/s.

Table 7 Thermophysical properties of water [50], $AgSiO_2$-eg [56] and Therminol-66 [60]

Thermophysical properties of water	Formula
Density/($kg·m^{-3}$)	$\rho(T) = \begin{cases} 6.31\times10^{-5}T^3 - 6.04\times10^{-2}T^2 + 18.92T - 950.70 & (273 \leqslant T \leqslant 293) \\ 1.03\times10^{-5}T^3 - 1.34\times10^{-2}T^2 + 4.97T + 432.26 & (293 < T \leqslant 373) \end{cases}$
Thermal conductivity/($W·(m·K)^{-1}$)	$k(T) = -0.87 + 8.95\times10^{-3}T - 1.58\times10^{-5}T^2 + 7.98\times10^{-9}T^3$
Specific heat capacity/($J·(kg·K)^{-1}$)	$c_p(T) = 12010.15 - 80.41T + 0.31T^2 - 5.38\times10^{-4}T^3 + 3.63\times10^{-7}T^4$
Dynamic viscosity/(Pa·s)	$\mu(T) = 2.79\times(1.38 - 2.12\times10^{-2}T + 1.36\times10^{-4}T^2 - 4.65\times10^{-7}T^3 + 8.90\times10^{-10}T^4 - 9.08\times10^{-13}T^5 + 3.85\times10^{-16}T^6$ $(273 \leqslant T \leqslant 413)$ $\mu(T) = 4.01\times10^{-3} - 2.11\times10^{-5}T + 3.86\times10^{-8}T^2 - 2.40\times10^{-11}T^3$ $(413 < T \leqslant 554)$
Thermophysical properties of $AgSiO_2$-eg	**Formula**
Density/($kg·m^{-3}$)	$\rho(T) = -0.0005511T^2 - 0.35518T + 1264.7843$
Thermal conductivity/($W·(m·K)^{-1}$)	$k(T) = -1.0966\times10^{-9}T^3 + 7.814\times10^{-7}T^2 - 0.0001076T + 0.24328$
Specific heat capacity/($J·(kg·K)^{-1}$)	$c_p(T) = -0.002692T^2 + 6.4563T + 727.9491$
Dynamic viscosity/(Pa·s)	$\mu(T) = 0.00148 + 132236.29666e^{-0.05352T}$
Thermophysical properties of Therminol-66	**Formula**
Density/($kg·m^{-3}$)	$\rho(T) = 1163.4 - 0.4366T - 0.0003T^2$
Thermal conductivity/($W·(m·K)^{-1}$)	$k(T) = 0.1153 + 5\times10^{-5}T - 2\times10^{-7}T^2$
Specific heat capacity/($J·(kg·K)^{-1}$)	$c_p(T) = 672.9 + 2.8T + 10^{-3}T^2$
Dynamic viscosity/(Pa·s)	$\mu(T) = 999.18 - 13.498T + 0.0749T^2 - 0.00025T^3 + 4\times10^{-7}T^4 - 3\times10^{-10}T^5 + 10^{-13}T^6$

Likewise, the radiative heat loss to the ambient can be modeled using the surface-to-surface interface in COMSOL. The sky temperature is calculated from [15]:

$$q_{\mathrm{r,loss}} = \varepsilon\sigma\left(T^4 - T_{\mathrm{sky}}^4\right), T_{\mathrm{sky}} = 0.0552T_{\mathrm{amb}}^{1.5}, \tag{23}$$

where T_{amb} and T_{sky} represent the ambient temperature and sky temperature, respectively.

To describe the thermal performance of the collector, we define two thermal efficiency measures, one relating to the filter channel ($\eta_{\mathrm{th-f}}$) and one to the primary channel ($\eta_{\mathrm{th-r}}$) as:

$$\eta_{\mathrm{th-f}} = \frac{\dot{m}_{\mathrm{f}} c_{\mathrm{pf}} \left(T_{\mathrm{fo-f}} - T_{\mathrm{fi-f}}\right)}{G_{\mathrm{AM1.5}} A_{\mathrm{c}}}, \tag{24}$$

$$\eta_{\mathrm{th-r}} = \frac{\dot{m}_{\mathrm{r}} c_{\mathrm{pr}} \left(T_{\mathrm{fo-r}} - T_{\mathrm{fi-r}}\right)}{G_{\mathrm{AM1.5}} A_{\mathrm{c}}}, \tag{25}$$

where $\dot{m}_{\mathrm{f}}$ and $\dot{m}_{\mathrm{r}}$ are the mass flow rates in the filter channel and in the primary channel, c_{pf} and c_{pr} are the specific heat capacities of the filter fluid and fluid in the primary channel, $T_{\mathrm{fo-f}}$ and $T_{\mathrm{fi-f}}$ are the outlet and inlet temperatures of the fluid through the filter channel, and $T_{\mathrm{fo-r}}$ and $T_{\mathrm{fi-r}}$ are the outlet and inlet temperatures of the fluid through the primary channel.

Furthermore, we define an overall thermal efficiency ($\eta_{\mathrm{th-o}}$):

$$\eta_{\mathrm{th-o}} = \eta_{\mathrm{th-f}} + \eta_{\mathrm{th-r}}, \tag{26}$$

which, however, needs to be interpreted carefully and in conjunction with the separate efficiency measures (Eqs. (24) and (25)), as the temperatures delivered the two channels may be different.

The thermal efficiency of the filter is considered a function of the reduced temperature $T_{\mathrm{r-f}}$:

$$T_{\mathrm{r-f}} = \frac{\frac{T_{\mathrm{fo-f}} + T_{\mathrm{fi-f}}}{2} - T_{\mathrm{amb}}}{G_{\mathrm{AM1.5}}}, \tag{27}$$

and similarly, we can attempt to relate the overall thermal efficiency of the collector to an average overall reduced temperature $T_{\mathrm{r-o}}$:

$$T_{\mathrm{r-o}} = \frac{\frac{\left(\frac{T_{\mathrm{fo-f}} + T_{\mathrm{fo-r}}}{2}\right) + \left(\frac{T_{\mathrm{fi-f}} + T_{\mathrm{fi-r}}}{2}\right)}{2} - T_{\mathrm{amb}}}{G_{\mathrm{AM1.5}}}. \tag{28}$$

A flowchart for the modeling and simulation of the SSCPV-T collector is shown in Fig. 6. The numerical simulation begins with optical modeling. A 2-D geometrical optics model (COMSOL) and a theoretical calculation (MATLAB code) are employed to evaluate the solar irradiance that falls on the PV surfaces and that is absorbed by the filter. Thereafter, both COMSOL and MATLAB models are compared to confirm their accuracy of prediction. Next, the MATLAB electrical model leverages the results obtained from the previous optical model to estimate the electrical performance of the solar cell when spectral splitting is considered. The electrical efficiency is initially calculated at the standard temperature of 25 °C (298 K) and is later corrected for the actual operating cell temperature. Finally, the 3-D COMSOL thermal-fluid model described above considers the optics results and

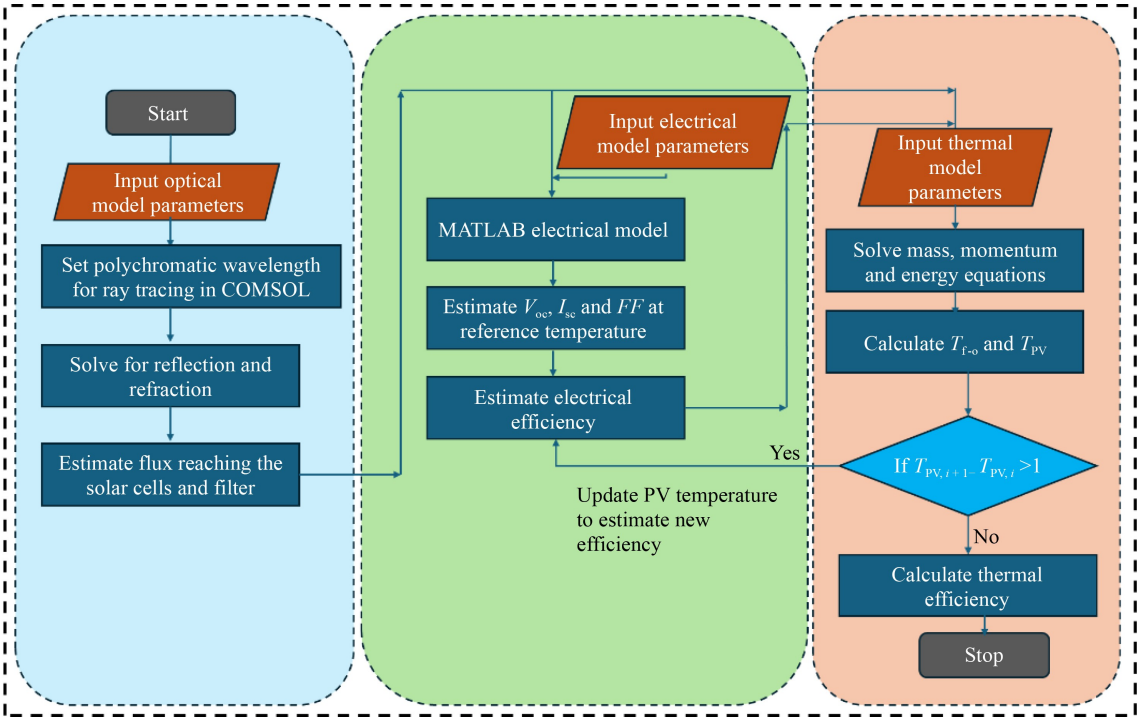

Fig. 6 Flowchart for simulating the spectral-splitting CPV-T collector.

electrical performance results, enabling the model to calculate the outlet temperature and thermal performance of the SSCPV-T collector. The PV surface temperature from the thermal model will then be utilised to calculate a more accurate electrical efficiency. After adjusting the electrical efficiency, it will be utilised as the input for the thermal model once more. This iterative approach helps in enhancing the accuracy of the electrical and thermal performance estimation of the collector.

3.4 Mesh independence study

In the present study, a segregated approach is adopted to split the problem into multiple physics-based steps, each solved iteratively following a predefined sequence. The iteration process continues until the relative change for all the variables associated with each step falls below a set tolerance of 10^{-4}. The solvers used in each step are presented in Table 8.

Table 8 Summary of solvers used in COMSOL settings

Segregated steps	Solver
Radiosity	PARDISO
Velocity u_1, pressure p_1 (laminar flow)	GMRES
Temperature	GMRES
Velocity u_2, pressure p_2 (turbulent flow)	PARDISO
Turbulence variables	PARDISO

The COMSOL simulations performed in the present study employ a finite element method, with an unstructured tetrahedral meshing scheme applied to all domains based on COMSOL's predefined physics-based settings to control the mesh size and element growth rate.

A mesh independence study was conducted in which we evaluated the outlet fluid temperature from the filter channel for given conditions: the incident irradiance was set to 1000 W/m^2, the wind speed was set to 1 m/s, the flow rate in the primary PV-T channel was set to 0.1 kg/s, the ambient temperature was maintained at 25 °C, the inlet temperature to the primary PV-T channel was also set to 25 °C, and the inlet temperature to the filter was set to 20 °C. The mesh density (number of elements) was varied from 1.6×10^5 to 4.5×10^5. The results, which are summarised in Table 9, indicate that increasing the number of elements changes the result of the simulation by no more than 0.2%. On this basis, the simulations used throughout this work employed 3.1×10^5 elements as a compromise between accuracy and acceptable computational resources. The meshed geometry of the collector used in the simulations is shown in Fig. 7.

4 Results and discussion

In this section, results relating to the performance of the SSCPV-T collector proposed in this study are presented and discussed. This section also includes validation of the optical, thermal-fluid and spectral-splitting models. Following validation against results taken from the literature, the proposed collector is studied, considering the effects of the filter fluid flow rate, the variation of the filter inlet temperature, and different filter fluids.

Table 9 Variation of filter outlet temperature and thermal efficiency with increasing number of mesh elements

No. of elements	Filter outlet temperature/°C	Thermal efficiency/%	Temperature deviation/%	Efficiency deviation/%
1.6×10^5	26.10	14.1	–	–
3.1×10^5	26.12	14.4	0.07	1.8
4.4×10^5	26.14	14.6	0.15	3.6
4.5×10^5	26.15	14.7	0.19	4.5

Notes: Conditions: irradiance = 1000 W/m2, wind speed = 1 m/s, primary PV-T channel flow rate = 0.1 kg/s, ambient temperature = 25 °C, primary PV-T channel inlet temperature = 25 °C, filter channel inlet temperature = 25 °C.

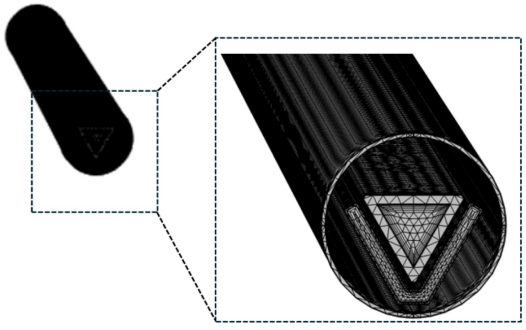

Fig. 7 Mesh generated for the CPV-T collector simulations.

4.1 Model validation

4.1.1 Optical model

The optical model in the present work was compared against results reported by Hou et al. [53], as these authors also considered a parabolic trough collector, whose geometry is shown in Fig. 8(a). For a fair comparison of the optical simulation results, the geometry and reflectivity of the parabolic reflector, and absorptivity of the flat plate receiver (at the top) were implemented in our model. A solar disk radial angle of 4.65 mrad was employed to simulate the finite size of the sun.

The distribution of the local concentration ratio (LCR) over the illuminated surface of the flat plate receiver is presented in Fig. 8(b), with the highest LCR obtained on the central symmetry axis, i.e., $x = 0$. The two distributions exhibit good agreement over most of the plotted range, with an acceptable divergence in the central area of the receiver (-2.5 mm $< x <$ 2.5 mm). The maximum LCR value is ~122 in Hou et al. [53], and ~117 in the present model results. This amounts to a

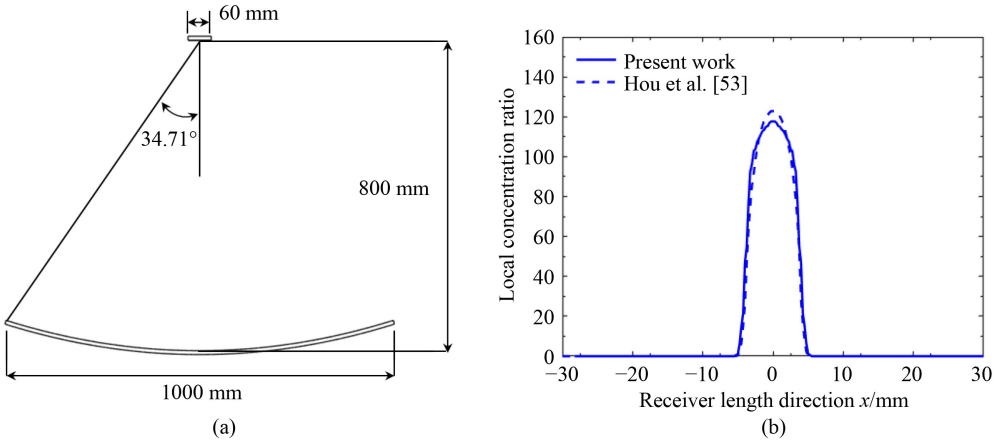

Fig. 8 (a) Geometrical configuration of the model used by Hou et al. (adapted with permission from Hou et al. [53], copyright 2023, Elsevier); (b) optics model comparison with results from the same study.

worst-case deviation of < 10%, which is considered acceptable for the present work.

4.1.2 Thermal-fluid model

Data from the experiments by Yousef et al. [62] were selected for validation of the coupled optical-electrical and thermal-fluid model. Specifically, Yousef et al. [62] tested a compound parabolic concentrator-based PV-T collector, whose details are shown in Fig. 9(a), under outdoor conditions in New Borg EI-Arab city, Egypt, situated at a latitude of 30°55′ North and a longitude of 29°42′ East. The hourly solar irradiance and wind speed were measured by a pyranometer and a portable meteorological weather station.

To simulate the sun's position based on real-world conditions, the solar radiation node was enabled in the COMSOL validation model, with specifications provided for the location, date, local time, solar irradiance, etc. The simulations were performed for steady-state conditions. The predicted average temperature on the PV surface is shown in Fig. 9 and the results are compared to the experiment data in Yousef et al. [62]. Our predictions show good agreement with the experiments of Yousef et al. [62] with a root mean square error (RMSE) < 8%.

4.1.3 Liquid absorptive filter model

Predictions from the liquid filter model developed in the present work were compared to results from Ju et al. [63], who examined a rectangular optical filter channel with a nanofluid (see Fig. 10(a)), namely indium tin oxide (ITO) dispersed in Therminol VP1, flowing inside the channel as the liquid absorptive medium. This nanofluid exhibits strong absorption characteristics at wavelengths > 1300 nm, while having a high transmittance in the visible spectrum [48].

To predict the electrical and thermal performance of this absorptive filter using our model in COMSOL Multiphysics, the incident solar radiation was considered a polychromatic source of light and a function of wavelength. Spectral splitting was implemented by

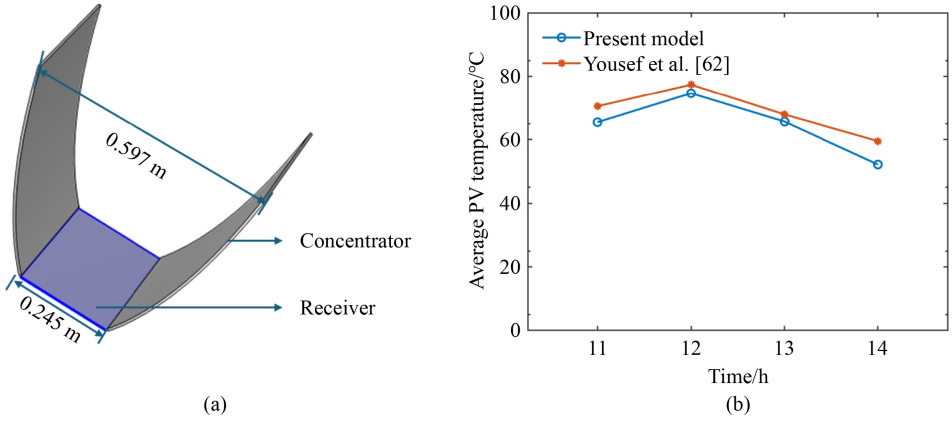

Fig. 9 (a) CPC concentrator used by Yousef et al. (adapted with permission from Yousef et al. [62], copyright 2016, Elsevier), and (b) thermal-fluid model validation via comparison with results from the same study.

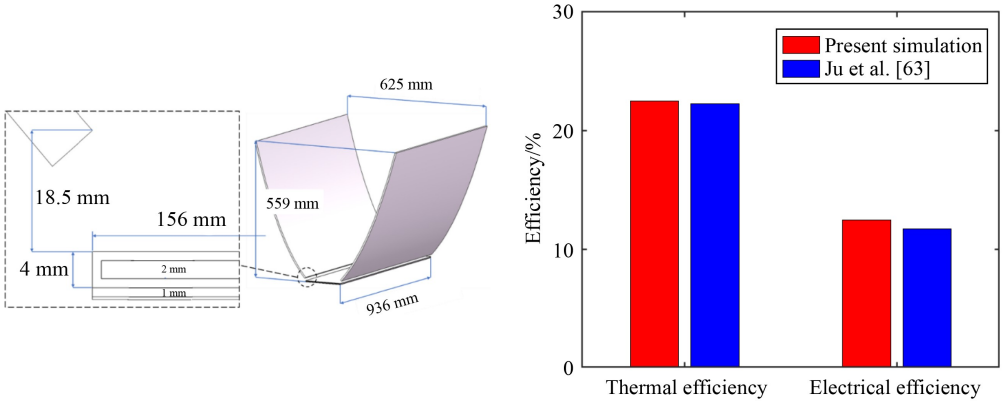

(a) (b)

Fig. 10 (a) Geometrical arrangement used by Ju et al. (adapted with permission from Ju et al. [63], copyright 2020, Elsevier); (b) filter model validation via comparison with results from the same study.

enabling a wall node at the surface of the liquid filter where the light first meets the liquid phase and activating an evaluation expression such that the spectrum from 280 to 1300 nm passes through this surface, while the rest is absorbed at this liquid surface. This was done by implementing a material discontinuity interface and specifying the average transmittance of the liquid over the range 280–1300 nm, whereas the non-transmitted portion of the spectrum was absorbed by the filter.

Using this model, the solar flux received by the solar cells was estimated to be 1980 W/m^2, and the solar flux absorbed by the filter was 1050 W/m^2. Subsequently, these values were applied as the inward heat fluxes on the upper surface of the PV cells and filter in the validation model.

In their study, Ju et al. [63] applied a uniform heat flux coupling method and estimated an electrical output of 68 W and a thermal output of 130 W in their optical filter. In the present work, and using our model, we predicted values of 73 and 131 W, respectively. The predictions obtained with the model in the present work show acceptable agreement with Ju et al. [63], with errors < 6% for the electrical and < 1% for the thermal output (and, also, efficiency) as shown in the Fig. 10.

It is important to be aware of some limitations in the validation effort of the filter model that arise from the fact that the SSCPV-T results made available by Ju et al. [63] were also generated using a numerical simulation model, however, this model was, in turn, validated based on direct comparison against experimental data reported in a previous study by Cui and Zhu [64].

4.2 Optical simulation results for SSCPV-T collector

A result from a 2-D COMSOL ray tracing simulation for the SSCPV-T collector proposed in this work (Figs. 1 and 4), using 1 × 10^6 polychromatic rays, is shown in Fig. 11(a). To generate these results, the transmittivity of the cover and filter glass and water were provided as inputs to COMSOL. The flux distribution around the primary channel surfaces is shown in Fig. 11(b).

A (symmetric) maximum local flux of ~12 kW/m^2 is

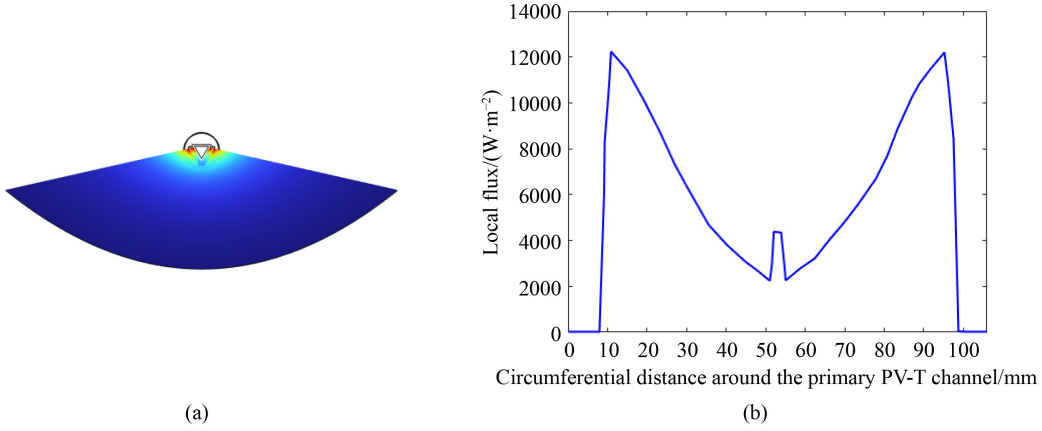

(a) (b)

Fig. 11 (a) Ray tracing for the SSCPV-T collector design; (b) local flux distribution around the circumferential distance around the primary PV-T channel.

found at 15 mm from the left/right edges of this distribution, which correspond to the two top corners of the primary PV-T channel or triangular channel. From 15 mm and up to 50 mm, a monotonic decrease in flux is observed down to ~2.5 kW/m^2. The average flux received by the primary channel is estimated at 5.7 kW/m^2, and the average flux absorbed by the filter at 1.3 kW/m^2. These fluxes were estimated by the COMSOL ray tracing software and were also checked against an in-house optical code written in MATLAB which showed similar predictions. A comparison of COMSOL and MATLAB results is given in Table 10.

Table 10 Comparison of optical simulation results from COMSOL and MATLAB

Parameter	Unit	MATLAB	COMSOL
Heat flux absorbed by the filter	W/m^2	1300	1280
Solar irradiance on PV	W/m^2	5750	5720

4.3 Effect of flow rate on collector performance

The effect of varying the flow rate of water in the filter on the electrical and thermal performance of the collector is shown in Fig. 12. For these simulations, the incident irradiance was set to 1000 W/m^2, the wind speed was set to 1 m/s, the flow rate in the primary PV-T channel was set to 0.1 kg/s, the ambient temperature was maintained at 25 °C, and the inlet temperature to the primary PV-T channel was also set to 25 °C. The mass flow rate in the filter was varied as a fraction of the mass flow rate in the primary PV-T channel.

As the mass flow ratio in the filter was increased, a decrease in outlet temperature and an increase in thermal efficiency is observed. Interestingly, the temperature of the PV cells and the electrical performance of the collector remain relatively unchanged; therefore, the variation in the overall thermal efficiency of the collector follows a similar trend to that of the filter. For a mass flow ratio of 0.033, the electrical efficiency is 15%, the overall thermal efficiency is 42%, and the thermal efficiency of the filter is 12% with an outlet temperature from the filter of ~60 °C. As the mass flow ratio in the filter increases, the electrical and thermal efficiencies plateau, which essentially means that any further increase in mass fraction results in a marginal improvement in the thermal and electrical efficiencies. This marginal improvement in the efficiencies comes at the expense of a significant increase in the pumping power inside the filter. Therefore, the mass flow ratio was capped at 0.24 for the rest of this study. For the estimation of the characteristic curve of the collector, a mass flow ratio of 0.2 was chosen for this study. The spatial temperature distribution over the filter of the SSCPV-T collector for two mass flow rates, i.e., 0.0011 kg/s or 4 L/h (LPH), and 0.02 kg/s or 72 LPH, is shown in Fig. 13, again demonstrating how, as the flow rate in the filter increases, the filter channel temperature and its variation decrease as expected.

4.4 Thermal performance of the filter

Figure 14 shows thermal performance of water as liquid filter where thermal efficiency of the filter is plotted against the reduced temperature of the filter. As the reduced temperature of the filter increases, the convective and radiative losses from the filter also increase resulting in a decrease in thermal performance. The reduced temperature at which the filter's thermal efficiency is zero is referred to as the stagnation temperature of the filter, thus the stagnation temperature is the maximum temperature that the filter can achieve. Similarly, the thermal efficiency at a reduced temperature of zero is the maximum efficiency that the filter can achieve.

To estimate the characteristic thermal efficiency curves of the filter, simulations were performed for an irradiance of 1000 W/m^2, wind speed of 1 m/s, ambient temperature

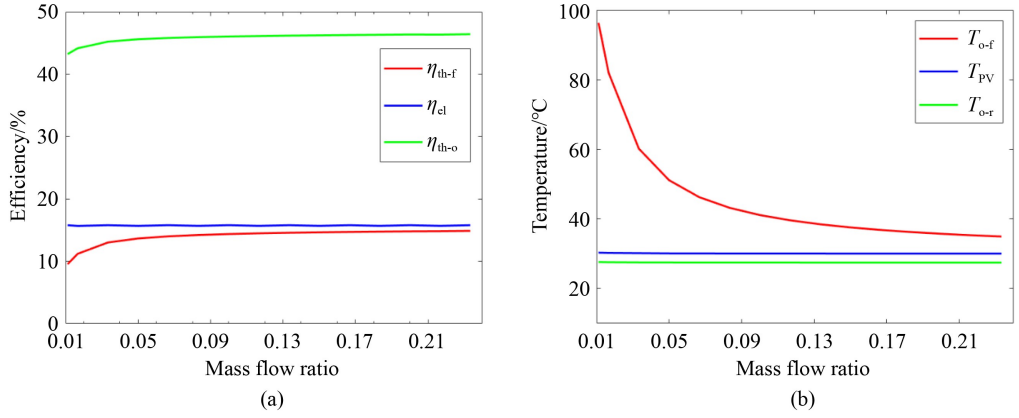

Fig. 12 Effect of variation of mass flow ratio in the filter.electrical efficiency. $T_{o\text{-}f}$: outlet temperature from the filter; T_{pv} : mean temperature of the PV cell; $T_{o\text{-}r}$: Outlet temperature from the receiver.

(a) Electrical and thermal efficiencies of the collector; (b) outlet fluid and PV cell temperatures.

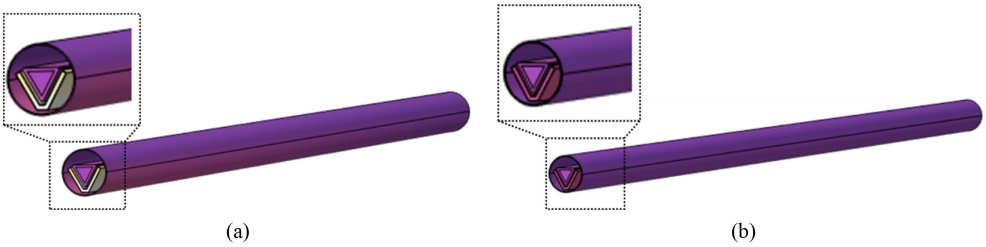

Fig. 13 Temperature distribution over the SSCPV-T primary channel.
(a) The mass flow rate is 4 LPH; (b) the mass flow rate is 72 LPH.

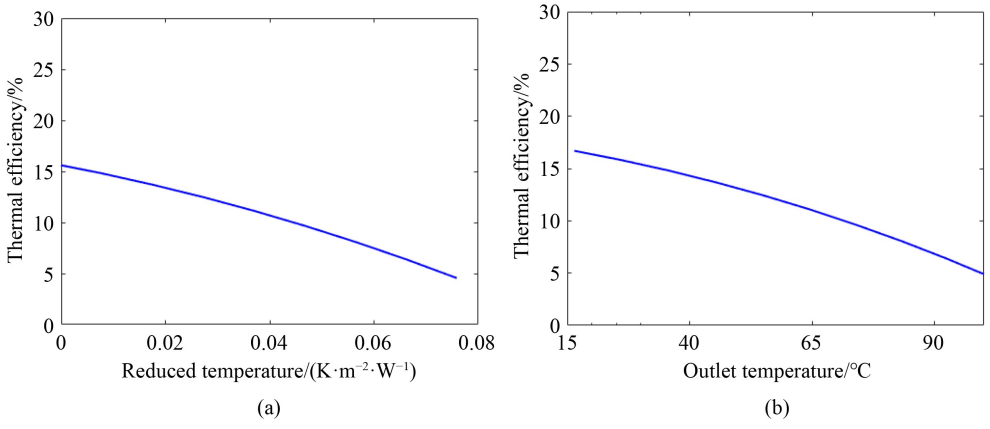

Fig. 14 Efficiencies of the filter varies with the following factors.
(a) Reduced temperature; (b) outlet water temperature from the filter channel.

of 25 °C, mass flow rates in the primary PV-T channel and filter of 0.1 and 0.02 kg/s (mass flow ratio of 0.2), and with the inlet water temperature to the primary PV-T channel fixed to 25 °C. Since the aim of this work is to achieve a high grade of thermal output from the filter without significantly affecting electrical performance, a high mass flow rate (0.1 kg/s) and constant inlet water temperature (25 °C) was maintained in the primary PV-T channel throughout the simulations. The reduced temperature of the filter channel was varied by increasing the inlet temperature in steps of 10 °C until the outlet temperature of the filter reached 100 °C. The simulation was stopped when outlet water temperature reached 100 °C as capturing two phase flow is beyond the scope of this work.

Figure 14(a) shows the thermal efficiency of the filter channel as a function of the corresponding reduced temperature. As expected, when the inlet temperature of the filter increases, the mean temperature of the filter also increases, thereby increasing heat losses and decreasing the thermal efficiency of the collector. At a reduced temperature of ~0.0045 $(K \cdot m^2)/W$, the thermal efficiency of the filter is observed to be ~15%, and the outlet temperature from the filter is 36 °C. As the reduced temperature of the filter increases to 0.075 $(K \cdot m^2)/W$, the thermal efficiency reduces to ~5% and the corresponding outlet temperature rises to ~100 °C, as shown in Fig. 14(b). The spatial distribution of temperature over the receiver, when the inlet water temperature to the filter channel is set to 20, 40 and 70 °C, is shown in Fig. 15.

4.5 Overall performance of the collector

A challenge in quantifying the overall performance of the collector arises from the different temperatures of the primary and filter channels. To overcome this challenge, we have defined, beyond the electrical efficiency, an overall thermal efficiency (sum of thermal efficiencies of the primary and filter channels) and an overall (average) reduced temperature measure that takes into account the average inlet and outlet temperatures of both channels. Simulations were performed for an irradiance of 1000 W/m^2, wind speed of 1 m/s, ambient temperature of 25 °C, mass flow rates in the primary channel and filter (water) of 0.1 and 0.02 kg/s (mass flow ratio of 0.2), and with the inlet water temperature to the primary PV-T channel fixed to 25 °C.

Figure 16 shows electrical and overall thermal performance curves for the SSCPV-T collector as a function of overall reduced temperature of the collector. At a reduced temperature of ~0 $(K \cdot m^2)/W$, the overall thermal efficiency of the collector is found to be ~46%, and the electrical efficiency is ~15%. Similarly, when reduced temperature increased to 0.038 $(K \cdot m^2)/W$, the

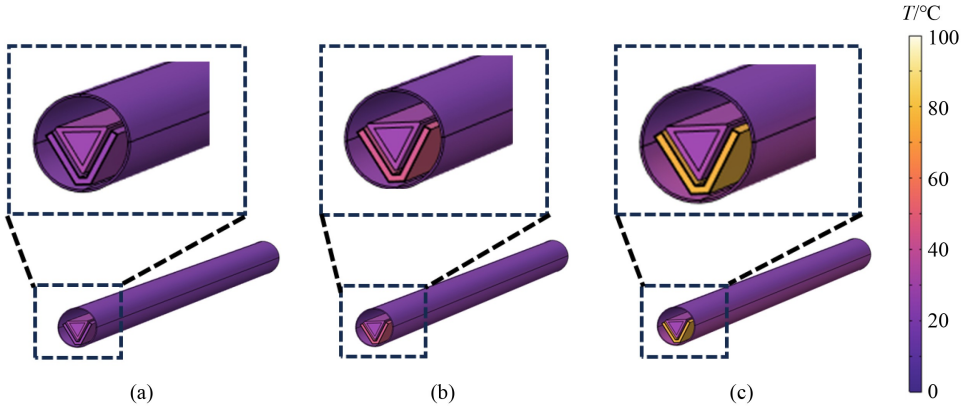

Fig. 15 Temperature distribution over the SSCPV-T collector when the inlet water temperature to the filter channel is: (a) 20 °C; (b) 40 °C; (c) 70 °C.

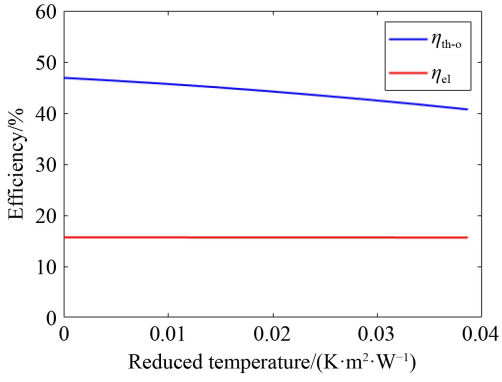

Fig. 16 Efficiencies of the collector as a function of reduced temperature for: irradiance of 1000 W/m^2, wind speed of 1 m/s, ambient temperature of 25 °C, mass flow rates in the primary channel and filter (water) of 0.1 and 0.02 kg/s (mass flow ratio of 0.2), and with the inlet water temperature to the primary channel fixed to 25 °C.

thermal efficiency dropped to 40% and electrical efficiency remained relatively constant at 15%.

4.6 Role of liquid filter

One of the challenges of using water as a SS filter is the outlet temperature, which is limited to (near) 100 °C to avoid boiling at (near) atmospheric pressure. The use of a HTF such as Therminol-66 can overcome this challenge. In addition, Therminol-66 and water are semi-transparent beyond 1100 nm, which detrimentally transmits part of the IR spectrum onto the solar cells, therefore a $AgSiO_2$-eg nanofluid that can block this has also been studied as a filter fluid.

The fractions of the incident solar energy that is converted to electricity, a thermal energy gain in the primary PV-T channel (for low-temperature heat) and the filter channel (for high-temperature heat) when using water, Therminol-66, or $AgSiO_2$-eg nanofluid as the filter material at a reduced temperature of 0 (K·m^2)/W, are shown in Fig. 17. The energy breakdowns for water and Therminol-66 as filters is similar, with both achieving an electrical efficiency of ~16%. This similarity in electrical efficiency is attributed to the relatively high transmittance (> 95%) of both materials within the wavelength range of 550–920 nm, which overlaps the spectral response of c-Si solar cells. For wavelengths below 550 nm, Therminol-66 demonstrates superior heat absorption, whereas water has higher absorption beyond 1200 nm. Although these liquids absorb radiation in different

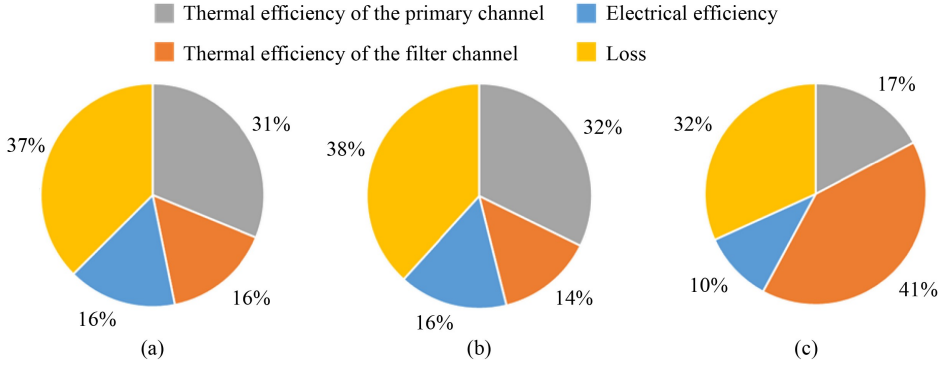

Fig. 17 Energy output breakdown for different liquid filter materials when the reduced temperature of the filter is at 0 (K·m^2)/W. (a) Water; (b) Therminol-66; (c) $AgSiO_2$-eg.

regions of the solar spectrum, the total absorbed radiation remains nearly identical, leading to similar thermal performance in the filter channel (16% for water and 14% for Therminol-66). In contrast, $AgSiO_2$-eg exhibits a distinct energy distribution: it achieves a much lower electrical efficiency of ~10%, but achieves a significantly higher thermal efficiency of close to 41% in the filter channel. The higher absorptivity of $AgSiO_2$-eg at wavelengths below 800 nm blocks a portion of the visible part of the spectrum from reaching the cells, thereby reducing the electrical efficiency, while enhancing the thermal performance in the filter. Thus, the use of $AgSiO_2$-eg as a SS filter prioritises high-temperature heat generation in the filter channel at the expense of the electricity output.

Results from a comparative study of these three alternatives, i.e., water, Therminol-66, and $AgSiO_2$-eg, as the SS filter are show in Fig. 18. From this figure, we can see that the use of $AgSiO_2$-eg as a filter fluid can improve the thermal efficiency of the filter by 2–3 times at a reduced temperature of 0 $(K \cdot m^2)/W$ compared to water or Therminol-66, and that the thermal efficiency of the filter when using $AgSiO_2$-eg is always higher than that attained with Therminol-66 or water.

The thermal efficiency of $AgSiO_2$-eg filter at a reduced temperature of 0.02 $(K \cdot m^2)/W$ is ~38% whereas the use of Therminol-66 and water leads to equivalent efficiency values of 11% and 12% respectively for the same reduced temperature. The improvement in thermal performance of $AgSiO_2$-eg filter can be attributed to the higher absorptivity of the nanofluid filter in the visible spectrum which, however, also leads to a decrease in electrical efficiency. The electrical efficiency in the case of a $AgSiO_2$-eg filter fluid is ~10% whereas for water and Therminol-66 this is ~15% as shown in Fig. 18(b). The overall maximum thermal efficiencies of the collector for the cases of water and Therminol-66 are ~45%, however, for the $AgSiO_2$-eg nanofluid this improves to ~60%.

A comparative study between Therminol-66 and water as the filter fluid reveals that the thermal efficiency when employing water is always higher, even though both fluids have similar total absorption. For a given inlet temperature, the increase in the outlet temperature when using Therminol-66 is always higher than with water, which can be attributed to the lower specific heat capacity of Therminol-66. The higher temperatures achieved with Therminol-66, lead to enhanced losses due to convection and radiation and, ultimately, a reduction in the thermal efficiency of the filter. Temperature distributions over the filter channel when using water, Therminol-66 and $AgSiO_2$-eg for inlet temperatures of 20 and 70 °C are shown in Fig. 19.

5 Conclusions

In this study, a novel SSCPV-T collector design has been proposed, with water, $AgSiO_2$-eg and Therminol-66 investigated as three potential optical filter fluids for spectral splitting. A coupled optical, electrical and thermal-fluid model was developed to estimate the electrical and thermal performance of the proposed collector. The optical model was developed in COMSOL Multiphysics 6.1 as a ray tracing tool followed by validation against an in-house MATLAB code. The results from the optical model were then used as inputs to the electrical model to estimate electrical performance, and subsequently, the outputs from the optical and electrical models were used as inputs to a thermal-fluid CFD model to estimate the thermal performance of the collector. Each sub-model model was independently validated against results published in the literature to check the accuracy of the model, with relative deviations < 10%.

Following these checks, a study on the performance of the SSCPV-T collector with water as the filter fluid was conducted. For this study, the flow rate in the filter fluid was varied as a fraction of the flow rate of the heat

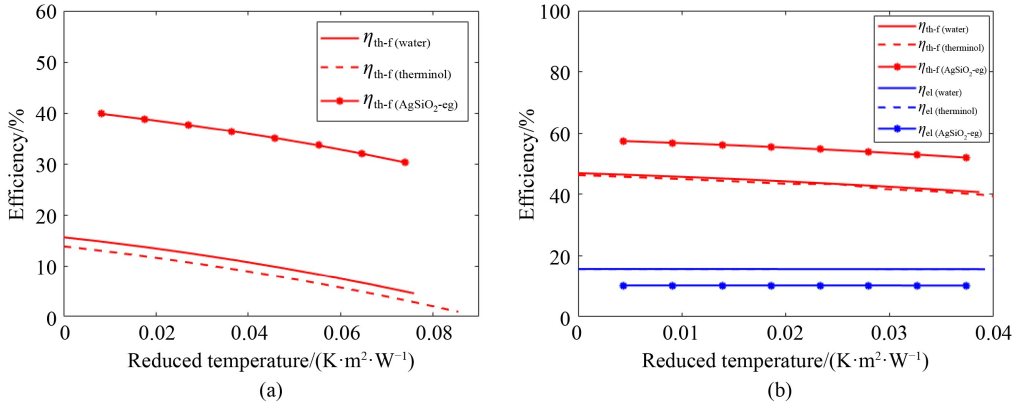

Fig. 18 Comparison of: (a) thermal efficiency of the filter channel as a function of reduced temperature, and (b) overall and electrical efficiencies as a function of reduced temperature for water, Therminol-66 and $AgSiO_2$-eg nanofluid as optical filter fluids.

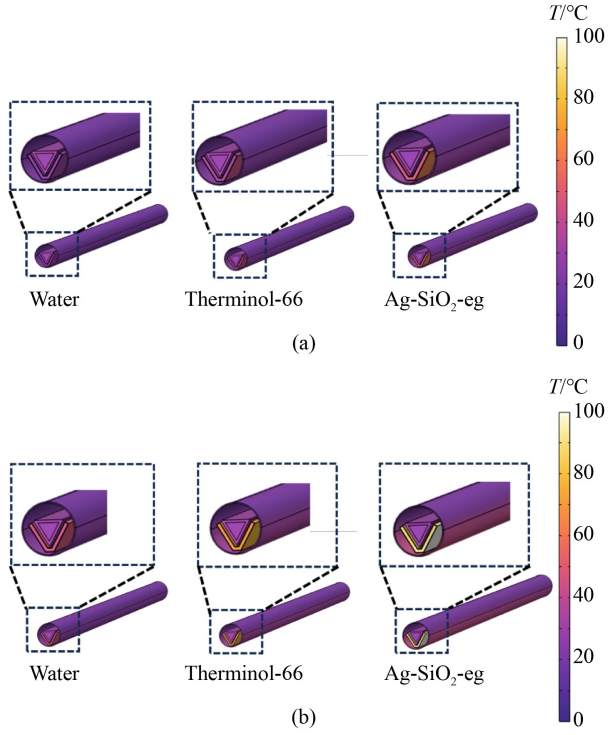

Fig. 19 Temperature distribution over the SSCPV-T collector filter with water, Therminol-66 and $AgSiO_2$-eg as optical filter fluids for different inlet temperature.
(a) 20 °C; (b) 70 °C.

transfer fluid in the primary PV-T channel. For an irradiance of 1000 W/m^2, an ambient temperature of 25 °C, a wind speed of 1 m/s, a water flow rate of 0.1 kg/s in the primary PV-T channel with an inlet temperature of 25 °C, and a water filter with a mass flow ratio of 0.2, the electrical efficiency was 15%, the maximum overall thermal efficiency was ~45% and the thermal efficiency of the filter was ~15%.

Furthermore, the performance of the SSCPV-T collector was explored by varying the water inlet temperature in the filter channel. Results reveal that for a water flow rate in the primary PV-T channel of 0.1 kg/s, a water flow rate in the filter channel of 0.02 kg/s, an inlet water temperature in the primary channel equal to the ambient temperature of 25 °C, the filter outlet temperature can easily reach 100 °C at 5% thermal efficiency, while the collector attains a 15% electrical efficiency and an overall thermal efficiency of 40%.

A comparison between water, $AgSiO_2$-eg and Therminol-66 as filter fluid reveals that $AgSiO_2$-eg improves the thermal efficiency of the filter channel by ~25% (absolute) compared to Therminol-66 and water, which also leads to a similar increase in the overall thermal efficiency of the collector, however, this improvement in thermal performance comes at an expense of a ~5% (absolute) electrical efficiency loss. If the thermal output of such a PV-T system is to be prioritised, this appears as a promising direction for overall performance improvement.

Notations

AM	Air mass
CFD	Computational fluid dynamics
CPV-T	Concentrating PV-T
HTC	Heat transfer coefficient
HTF	Heat transfer fluid
SS	Spectral splitting
SSPV-T	Spectral splitting PV-T
PV-T	Photovoltaic-thermal
PCM	Phase change material
A_c	Aperture area/m^2
A_{cell}	Area of cell/m^2
A_{cs}	Area of cross-section/m^2
A_i	Ideality factor
c	Speed of light/(m·s^{-1})
c_{pf}	Specific heat capacity filter/(J·(kg·K)$^{-1}$)
c_{pr}	Specific heat capacity receiver/(J·(kg·K)$^{-1}$)
C_{geo}	Concentration ratio
D_f	Gap between filter and channel/m
D_H	Hydraulic diameter/m
D_o	Outer diameter of cover glass/m
e	Unit charge of electron/C
E_{bg}	Band gap energy/eV
f	Focal length/m
F	External force/N
FF	Fill factor
$G_{AM1.5}$	AM 1.5G irradiance/(W·m^{-2})
G_{pv}	Irradiance received by PV cell/(W·m^{-2})
H	Planck's constant/(J·s)
h_{wind}	Convective HTC due to wind/(W·(m^2·K)$^{-1}$)
I_{sc}	Short circuit current/A
J_{ds}	Dark saturation current density/(A·m^{-2})
J_{sc}	Short circuit current density/(A·m^{-2})
k_b	Boltzmann constant/(J·K^{-1})
k_s	Thermal conductivity of solid/(W/(m·K)$^{-1}$)
$\dot{m}$	Mass flow rate/(kg·s^{-1})
P	Pressure/(N·m^{-2})
P_w	Wetted perimeter/m
q	Conduction heat transfer flux/(W·m^{-2})
q_{conv}	Convective HTC/(W·(m^2·K)$^{-1}$)
q_{fl}	Heat flux absorbed by filter/(W·m^{-2})

q_{pv}	Heat flux absorbed by PV cell/(W·m^{-2})
q_r	Radiative heat flux/(W·m^{-2})
q_{vd}	Viscous dissipation flux/(W·m^{-2})
Re	Reynolds number
SR	PV cell spectral response/(A·W^{-1})
T	Temperature/K
T_{amb}	Ambient temperature/K
T_c	Cell temperature/K
$T_{in\text{-}f}$	Inlet temperature of filter/K
$T_{in\text{-}r}$	Inlet temperature of primary PV-T channel/K
$T_{out\text{-}f}$	Outlet temperature filter/K
$T_{out\text{-}r}$	Outlet temperature of primary PV-T channel/K
$T_{r\text{-}f}$	Reduced temperature filter/((K·m^2) ·W^{-1})
$T_{r\text{-}o}$	Reduced temperature overall/((K·m^2) ·W^{-1})
T_{sky}	Sky temperature/K
T_{std}	Standard operating cell temperature/K
t_c	Thickness of primary PV-T channel/m
t_f	Thickness of liquid filter/m
t_g	Thickness of cover glass/m
u, U	Fluid/bulk fluid velocity/(m·s^{-1})
V_{oc}	Open circuit voltage/V
V_{wind}	Wind velocity/(m·s^{-1})
w_i, w_o	Inner/outer width of primary PV-T channel/m
α_{pv}	Absorptivity of PV cell
β	Temperature coefficient/K^{-1}
ε	Emissivity
$\eta_{th\text{-}f}$	Thermal efficiency filter
$\eta_{th\text{-}o}$	Overall thermal efficiency
η_{el}	Electrical efficiency
λ	Wavelength/m
μ	Dynamic viscosity/((N·s) ·m^{-2})
ρ	Density/(kg·m^{-3})
ρ_c	Reflectivity of mirror
σ	Stefan–Boltzmann constant/(W·m^{-2}·K^{-4})
τ_g	Transmittivity of glass
τ_{fl}	Transmittivity of filter
θ	Angle

Acknowledgements This work was supported by the UK Engineering and Physical Sciences Research Council (EPSRC) (Grant No. EP/R045518/1), the Royal Society under an International Collaboration Award 2020 (Grant No. ICA\R1\201302), and UK company Solar Flow Ltd. This work has also been funded by the European Union under the SPECTRUM project (Grant Agreement No. 101172891). Partial support for this research was provided by Tecnologico de Monterrey Challenge-Based Research Funding Program. Data supporting this publication can be obtained on request from cep-laboratory@imperial.ac.uk. For the purpose of Open Access, the authors have applied a CC BY public copyright license to any Author Accepted Manuscript version arising from this submission.

Competing Interests The authors declare that they have no competing interests.

Open Access This article is licensed under a Creative Commons Attribution 4.0 International License, which permits use, sharing, adaptation, distribution and reproduction in any medium or format, as long as you give appropriate credit to the original author(s) and the source, provide a link to the Creative Commons licence, and indicate if changes were made. The images or other third party material in this article are included in the article's Creative Commons licence, unless indicated otherwise in a credit line to the material. If material is not included in the article's Creative Commons licence and your intended use is not permitted by statutory regulation or exceeds the permitted use, you will need to obtain permission directly from the copyright holder. To view a copy of this licence, visit http://creativecommons.org/licenses/by/4.0/.

References

1. Sharif A, Meo M S, Chowdhury M A F, et al. Role of solar energy in reducing ecological footprints: An empirical analysis. Journal of Cleaner Production, 2021, 292: 126028
2. Spyridonidou S, Vagiona D G. A systematic review of site-selection procedures of PV and CSP technologies. Energy Reports, 2023, 9: 2947–2979
3. Duffie J A, Beckman W A, McGowan J. Solar engineering of thermal processes. American Journal of Physics, 1985, 53: 382
4. Sarangi A, Sarangi A, Sahoo S S, et al. A review of different working fluids used in the receiver tube of parabolic trough solar collector. Journal of Thermal Analysis and Calorimetry, 2023, 148(10): 3929–3954
5. Herrando M, Pantaleo A M, Wang K, et al. Solar combined cooling, heating and power systems based on hybrid PVT, PV or solar-thermal collectors for building applications. Renewable Energy, 2019, 143: 637–647
6. Freeman J, Markides C N. A solar diffusion-absorption refrigeration system for off-grid cold-chain provision, Part II: System simulation and assessment of performance. Renewable Energy, 2024, 230: 120717
7. Ray S, Tripathy A K, Sahoo S S, et al. Effect of inlet temperature of heat transfer fluid and wind velocity on the performance of parabolic trough solar collector receiver: A computational study. International Journal of Heat and Technology, 2019, 37(1): 48–58
8. Cuce P M, Guclu T, Cuce E. Design, modelling, environmental, economic and performance analysis of parabolic trough solar collector (PTC) based cogeneration systems assisted by thermoelectric generators (TEGs). Sustainable Energy Technologies and Assessments, 2024, 64: 103745
9. Huang G, Markides C N. Spectral-splitting hybrid PV-thermal (PV-T) solar collectors employing semi-transparent solar cells as optical filters. Energy Conversion and Management, 2021, 248: 114776
10. Huang G, Wang K, Markides C N. Efficiency limits of concentrating spectral-splitting hybrid photovoltaic-thermal (PV-T) solar collectors and systems. Light, Science & Applications, 2021, 10(1): 28

11. Herrando M, Markides C N, Hellgardt K. A UK-based assessment of hybrid PV and solar-thermal systems for domestic heating and power: System performance. Applied Energy, 2014, 122: 288–309
12. Chandan S V, Suresh V, Iqbal S M, et al. 3-D numerical modelling and experimental investigation of coupled photovoltaic thermal and flat plate collector. Solar Energy, 2021, 224: 195–209
13. Peacock J, Huang G, Song J, et al. Techno-economic assessment of integrated spectral-beam-splitting photovoltaic-thermal (PV-T) and organic Rankine cycle (ORC) systems. Energy Conversion and Management, 2022, 269: 116071
14. Herrando M, Wang K, Huang G, et al. A review of solar hybrid photovoltaic-thermal (PV-T) collectors and systems. Progress in Energy and Combustion Science, 2023, 97: 101072
15. Chandan, Dey S, Md Iqbal S, et al. Numerical modelling and performance assessment of elongated compound parabolic concentrator based LCPVT system. Renewable Energy, 2021, 167: 199–216
16. Chandan D S, Kumar P S, Reddy K S, et al. Optical and electrical performance investigation of truncated 3X non-imaging low concentrating photovoltaic-thermal systems. Energy Conversion and Management, 2020, 220(113056): 113056
17. Chandan B H, Tahir A A, Reddy K S, et al. Performance improvement of a desiccant based cooling system by mitigation of non-uniform illumination on the coupled low concentrating photovoltaic thermal units. Energy Conversion and Management, 2022, 257: 115438
18. Acosta-Pazmiño I P, García-Ramos R A, Rivera-Solorio C I, et al. Development and testing of a low-concentrating photovoltaic-thermal collector. In: Proceedings of SolarPACES 2023, 29th International Conference on Concentrating Solar Power, Thermal, and Chemical Energy Systems, 2024
19. Pandey C, Wu M, Yildizhan H, et al. Modelling of a CPV-T collector for combined heat and power generation. In: Proceedings of Solar World Congress, International Solar Energy Society, 2023
20. Daneshazarian R, Cuce E, Cuce P M, et al. Concentrating photovoltaic thermal (CPVT) collectors and systems: Theory, performance assessment and applications. Renewable & Sustainable Energy Reviews, 2018, 81: 473–492
21. Li J, Zhang W, Xie L, et al. A hybrid photovoltaic and water/air based thermal (PVT) solar energy collector with integrated PCM for building application. Renewable Energy, 2022, 199: 662–671
22. Leonforte F, Miglioli A, Del Pero C, et al. Design and performance monitoring of a novel photovoltaic-thermal solar-assisted heat pump system for residential applications. Applied Thermal Engineering, 2022, 210: 118304
23. Kumar L, Hasanuzzaman M, Rahim N A, et al. Modeling, simulation and outdoor experimental performance analysis of a solar-assisted process heating system for industrial process heat. Renewable Energy, 2021, 164: 656–673
24. Ju X, Xu C, Liao Z, et al. A review of concentrated photovoltaic-thermal (CPVT) hybrid solar systems with waste heat recovery (WHR). Science Bulletin, 2017, 62(20): 1388–1426
25. He W, Huang G, Markides C N. Synergies and potential of hybrid solar photovoltaic-thermal desalination technologies. Desalination, 2023, 552: 116424
26. Pan X, Ju X, Yuan M, et al. Energy tracing of solar cells for spectral-beam-splitting photovoltaic/thermal (PVT) systems. Applied Energy, 2023, 345: 121320
27. Imenes A G, Mills D R. Spectral beam splitting technology for increased conversion efficiency in solar concentrating systems: A review. Solar Energy Materials and Solar Cells, 2004, 84(1–4): 19–69
28. Huang G, Wang K, Curt S R, et al. On the performance of concentrating fluid-based spectral-splitting hybrid PV-thermal (PV-T) solar collectors. Renewable Energy, 2021, 174: 590–605
29. Han X, Tu L, Sun Y. A spectrally splitting concentrating PV/T system using combined absorption optical filter and linear Fresnel reflector concentrator. Solar Energy, 2021, 223: 168–181
30. Han X, Chen X, Wang Q, et al. Investigation of $CoSO_4$-based Ag nanofluids as spectral beam splitters for hybrid PV/T applications. Solar Energy, 2019, 177: 387–394
31. Barthwal M, Rakshit D. Holistic opto-thermo-electrical analysis of a novel spectral beam splitting-based concentrating photovoltaic thermal system. Journal of Cleaner Production, 2022, 379: 134545
32. Liu Y, Hu P, Zhang Q, et al. Thermodynamic and optical analysis for a CPV/T hybrid system with beam splitter and fully tracked linear Fresnel reflector concentrator utilizing sloped panels. Solar Energy, 2014, 103: 191–199
33. Looser R, Vivar M, Everett V. Spectral characterisation and long-term performance analysis of various commercial heat transfer fluids (HTF) as direct-absorption filters for CPV-T beam-splitting applications. Applied Energy, 2014, 113: 1496–1511
34. Mojiri A, Stanley C, Rosengarten G. A high temperature hybrid photovoltaic-thermal receiver employing spectral beam splitting for linear solar concentrators. In: Proceedings Volume 9559, High and Low Concentrator Systems for Solar Energy Applications X, SPIE, 2015
35. Mojiri A, Stanley C, Taylor R A, et al. A spectrally splitting photovoltaic-thermal hybrid receiver utilising direct absorption and wave interference light filtering. Solar Energy Materials and Solar Cells, 2015, 139: 71–80
36. Stanley C, Mojiri A, Rahat M, et al. Performance testing of a spectral beam splitting hybrid PVT solar receiver for linear concentrators. Applied Energy, 2016, 168: 303–313
37. Widyolar B, Jiang L, Winston R. Spectral beam splitting in hybrid PV/T parabolic trough systems for power generation. Applied Energy, 2018, 209: 236–250
38. Joshi S S, Dhoble A S. Analytical approach for performance estimation of BSPVT system with liquid spectrum filters. Energy, 2018, 157: 778–791
39. Han X, Xue D, Zheng J, et al. Spectral characterization of spectrally selective liquid absorption filters and exploring their effects on concentrator solar cells. Renewable Energy, 2019, 131: 938–945
40. Li H, He Y, Wang C, et al. Tunable thermal and electricity generation enabled by spectrally selective absorption nanoparticles for photovoltaic/thermal applications. Applied Energy, 2019, 236: 117–126

41. Wingert R, O'Hern H, Orosz M, et al. Spectral beam splitting retrofit for hybrid PV/T using existing parabolic trough power plants for enhanced power output. Solar Energy, 2020, 202: 1–9
42. Yazdanifard F, Ameri M, Taylor R A. Numerical modeling of a concentrated photovoltaic/thermal system which utilizes a PCM and nanofluid spectral splitting. Energy Conversion and Management, 2020, 215: 112927
43. Ling Y, Li W, Jin J, et al. A spectral-splitting photovoltaic-thermochemical system for energy storage and solar power generation. Applied Energy, 2020, 260: 113631
44. Alnajideen M, Min G. Hybrid photovoltaic-thermoelectric system using a novel spectral splitting solar concentrator. Energy Conversion and Management, 2022, 251: 114981
45. Wang G, Zhang Z, Jiang T, et al. Thermodynamic and optical analyses of a novel solar CPVT system based on parabolic trough concentrator and nanofluid spectral filter. Case Studies in Thermal Engineering, 2022, 33: 101948
46. Meraje W C, Huang C C, Barman J, et al. Design and experimental study of a Fresnel lens-based concentrated photovoltaic thermal system integrated with nanofluid spectral splitter. Energy Conversion and Management, 2022, 258: 115455
47. Li J, Yang Z, Wang Y, et al. A novel non-confocal two-stage dish concentrating photovoltaic/thermal hybrid system utilizing spectral beam splitting technology: Optical and thermal performance investigations. Renewable Energy, 2023, 206: 609–622
48. Zhang Z, Zhang F, Zhang W, et al. Spectral-splitting concentrator agrivoltaics for higher hybrid solar energy conversion efficiency. Energy Conversion and Management, 2023, 276: 116567
49. Chougule S S, Srivastava A, Bolegave G G, et al. Next-generation solar technologies: Unlocking the potential of Ag-ZnO hybrid nanofluids for enhanced spectral-splitting photovoltaic-thermal systems. Renewable Energy, 2024, 236: 121405
50. COMSOL Inc. COMSOL Multiphysics Reference Manual, version: 6.1. 2025-03-24
51. The MathWorks, Inc. MATLAB Version: (R2022a). 2025-03-24
52. Inventive Power. Solar energy for industry. 2024-09-17
53. Hou Y, Yu X, Yang B, et al. Optical performance investigation on flat receiver for parabolic trough solar collector based on the MCRT method. Renewable Energy, 2023, 202: 525–536
54. Al Shehri A, Parrott B, Carrasco P, et al. Impact of dust deposition and brush-based dry cleaning on glass transmittance for PV modules applications. Solar Energy, 2016, 135: 317–324
55. Han X, Guo Y, Wang Q, et al. Optical characterization and durability of immersion cooling liquids for high concentration III–V photovoltaic systems. Solar Energy Materials and Solar Cells, 2018, 174: 124–131
56. Ma Y, Han X, Chen Z, et al. Performance analysis of a nanofluid spectral splitting concentrating PV/T system with triangular receiver based on MCRT-FVM coupled method. Applied Thermal Engineering, 2024, 239: 122096
57. Huang G, Curt S R, Wang K, et al. Challenges and opportunities for nanomaterials in spectral splitting for high-performance hybrid solar photovoltaic-thermal applications: A review. Nano Materials Science, 2020, 2(3): 183–203
58. SunPower Ltd. C60 monocrystalline silicon solar cell. 2024-09-22
59. Incropera F P, Dewitt D P, Bergman T L, et al. Fundamentals of Heat and Mass Transfer. New York: John Wiley & Sons Inc, 2001
60. Rajan A, Reddy K S. Integrated optical and thermal model to investigate the performance of a solar parabolic dish collector coupled with a cavity receiver. Renewable Energy, 2023, 219: 119376
61. Radwan A, Ahmed M, Ookawara S. Performance enhancement of concentrated photovoltaic systems using a microchannel heat sink with nanofluids. Energy Conversion and Management, 2016, 119: 289–303
62. Yousef M S, Abdel Rahman A K, Ookawara S. Performance investigation of low-concentration photovoltaic systems under hot and arid conditions: Experimental and numerical results. Energy Conversion and Management, 2016, 128: 82–94
63. Ju X, Abd El-Samie M M, Xu C, et al. A fully coupled numerical simulation of a hybrid concentrated photovoltaic/thermal system that employs a therminol VP-1 based nanofluid as a spectral beam filter. Applied Energy, 2020, 264: 114701
64. Cui Y, Zhu Q. Study of photovoltaic/thermal systems with MgO-water nanofluids flowing over silicon solar cells. In: 2011 Asia-Pacific Power and Energy Engineering Conference, Shanghai, China, 2012